Materials Horizons

ROYAL SOCIETY OF CHEMISTRY

COMMUNICATION

View Article Online
View Journal | View Issue

Cite this: *Mater. Horiz.*, 2024, 11, 2494

Received 27th January 2024,
Accepted 6th March 2024

DOI: 10.1039/d4mh00098f

rsc.li/materials-horizons

Multiple neighboring active sites of an atomically precise copper nanocluster catalyst for efficient bond-forming reactions†

Atanu Ghosh,‡[a] Arunachalam Sagadevan, ‡[a] Kathiravan Murugesan, [a] Stefan Adrian F. Nastase, [a] Bholanath Maity, [a] Mohammad Bodiuzzaman, [a] Aleksander Shkurenko, [b] Mohamed Nejib Hedhili, [c] Jun Yin, [d] Omar F. Mohammed, [b] Mohamed Eddaoudi, [b] Luigi Cavallo, [a] Magnus Rueping *[a] and Osman M. Bakr *[a]

Atomically precise copper nanoclusters (NCs) are an emerging class of nanomaterials for catalysis. Their versatile core–shell architecture opens the possibility of tailoring their catalytically active sites. Here, we introduce a core–shell copper nanocluster (CuNC), $[Cu_{29}(S^tBu)_{13}Cl_5(PPh_3)_4H_{10}]^tBuSO_3$ (S^tBu: *tert*-butylthiol; PPh_3: triphenylphosphine), Cu_{29}NC, with multiple accessible active sites on its shell. We show that this nanocluster is a versatile catalyst for C-heteroatom bond formation (C–O, C–N, and C–S) with several advantages over previous Cu systems. When supported, the cluster can also be reused as a heterogeneous catalyst without losing its efficiency, making it a hybrid homogeneous and heterogeneous catalyst. We elucidated the atomic-level mechanism of the catalysis using density functional theory (DFT) calculations based on the single crystal structure. We found that the cooperative action of multiple neighboring active sites is essential for the catalyst's efficiency. The calculations also revealed that oxidative addition is the rate-limiting step that is facilitated by the neighboring active sites of the Cu_{29}NC, which highlights a unique advantage of nanoclusters over traditional copper catalysts. Our results demonstrate the potential of nanoclusters for enabling the rational atomically precise design and investigation of multi-site catalysts.

New concepts

In the realm of modern synthetic chemistry, the focus is on developing efficient catalysts with well-defined active sites. Nanostructured materials, like metal nanoparticles, show promise, but their ill-defined structure hinders mechanistic understanding. Atomically precise nanoclusters (NCs), especially copper nanoclusters (CuNCs), with defined structures, offer a solution. Earth-abundant and cost-effective, CuNCs are emerging materials for sustainable catalysis applications. This work introduces a novel core–shell copper nanocluster, Cu_{29}NC, with a unique shell structure, demonstrating its efficiency in diverse C-heteroatom (C–O, C–N & C–S) bond-forming reactions. Unlike previous CuNCs, Cu_{29}NC serves as a recyclable and external ligand-free catalyst for a broad range of reactions, including late-stage functionalization of complex organic molecules. Experimental and theoretical investigations provide insights into its multi-site catalytic mechanism. We anticipate that the new insights gained from this study will be instrumental in the design, synthesis, and applications of more effective nanocluster catalysts for challenging bonding-forming reactions.

Introduction

Carbon-heteroatom (C-heteroatom) bond-forming reactions have played a pivotal role in organic transformations for the synthesis of pharmaceutical compounds, natural products, and organic materials.[1–7] Pd-catalyzed Buchwald–Hartwig reactions are among the most efficient methods for C-heteroatom cross-couplings.[8–11] However, the high cost of the metal as well as ligands hampers their widespread catalytic applications.[8,12] Accordingly, the copper-mediated Ullmann–Goldberg protocol[13] was devised as a potential cost-effective alternative but often suffered from the usage of stoichiometric amounts of copper and high reaction temperatures (>150 °C).[14,15] More recently, the groups of Buchwald,[16,17] Hartwig,[18] and Ma[19–22] have pioneered the use of copper catalysts with several ligand scaffolds (including neutral to anionic) to facilitate the cross-coupling reaction efficiently with a broader substrate scope.[23–26] However, as these Cu-catalyzed cross-coupling reactions require

[a] *KAUST Catalysis Center (KCC), Division of Physical Sciences and Engineering, King Abdullah University of Science and Technology (KAUST), Thuwal 23955-6900, Saudi Arabia. E-mail: osman.bakr@kaust.edu.sa, magnus.rueping@kaust.edu.sa*
[b] *Advanced Membranes and Porous Materials Center (AMPMC), Physical Sciences and Engineering Division, King Abdullah University of Science and Technology (KAUST), Thuwal 23955-6900, Saudi Arabia*
[c] *Core Labs, King Abdullah University of Science and Technology (KAUST), Thuwal 23955-6900, Kingdom of Saudi Arabia*
[d] *Department of Applied Physics, The Hong Kong Polytechnic University, Hung Hom, Kowloon, 999077, Hong Kong, China*

† Electronic supplementary information (ESI) available. CCDC 2292096. For ESI and crystallographic data in CIF or other electronic format see DOI: https://doi.org/10.1039/d4mh00098f

‡ These authors contributed equally to the work.

ligands – often in excess amounts[26–28] – they generate undesired ligand-related waste and may complicate the isolation process. Therefore, there is a pressing need to develop a new catalyst that can demonstrate efficient C-heteroatom coupling reactions without exogenous ligands.

A central objective in modern synthetic chemistry is the development of new and efficient catalysts for challenging bond-forming reactions – catalysts which should also have well-defined multiple active sites and are reusable.[29–31] Owing to their higher surface area, multiple active sites, and heterogenous nature, nanostructured materials (*e.g.*, metal nanoparticles, MNPs) have shown great potential for catalytic performance as compared to traditional homogenous catalysts.[32–38] However, due to their ill-defined structure it is difficult to delineate the role of active sites in the reaction mechanism and, hence, a catalysis-by-design approach cannot be practically implemented in such systems.[39] On the other hand, atomically precise nanoclusters (NCs, <3 nm), featuring well-defined positions of metal and ligands while possessing diverse polyhedral structures,[39–41] could serve as an ideal catalytic platform to enable the bond-forming reactions with mechanistic understanding owing to their structurally defined multiple active sites and tolerability for recycling. In particular, the catalytic properties of NCs highly depends on the nature of the protecting ligand and motif structure.[42–45]

To date, the structure–property relationships of nanocluster catalysts have mainly focused on precious metal nanoclusters such as Au and its alloys with Pd, Pt, and Ag for various chemical reactions.[39,40,43,46] Due to their earth abundance, cost-effectiveness, and versatile ligand architecture, copper nanoclusters have recently emerged for sustainable catalysis of chemical reactions.[37,47–53] The challenge in the development of new core–shell copper nanoclusters (CuNCs) that facilitate unique bond-forming reactions lies not only in their synthesis, but also in the unravelling of the reaction mechanism through atomically precise structure–property relationships of the CuNCs.

Herein we have designed and synthesized a novel core–shell copper nanocluster, $[Cu_{29}(S^tBu)_{13}Cl_5(PPh_3)_4H_{10}]^tBuSO_3$, ($Cu_{29}NC$) with a high percentage of chloride ligands on the surface. It encompasses a centred cubooctahedron core (Cu_{13}), shielded by a unique tetrahedral shell, $Cu_{16}S_{13}Cl_5P_4$. This shell is characterized by three distinct motifs, each exhibiting crown-like structures. The incorporation of chloride ligands in the shell serves to alleviate crowding around the active sites, making it a viable catalyst in organic reactions. We demonstrate that $Cu_{29}NC$ serves as an efficient catalyst to enable the broad range of cross-coupling reactions (C–O, C–N, and C–S) with a high functional group tolerance (Fig. 1). In contrast to previous Cu NCs, such as $Cu_{61}NC$ and $Cu_{28}NC$, which have proven effective as photocatalysts for certain cross-coupling reactions,[52,54] this $Cu_{29}NC$ serve as a recyclable external ligand-free catalyst for a broad range of C-heteroatom coupling reactions, including late-stage functionalization of complex organic molecules. A combined experimental investigation (with various controls) with theoretical DFT modeling (based on the single crystal structure) indicate the participation of multiple neighboring metal atoms in all fundamental steps of the reaction. This work opens new avenues for copper nanocluster-based catalysis and sheds light on their catalytic mechanism by DFT calculation based on the single crystal structure.

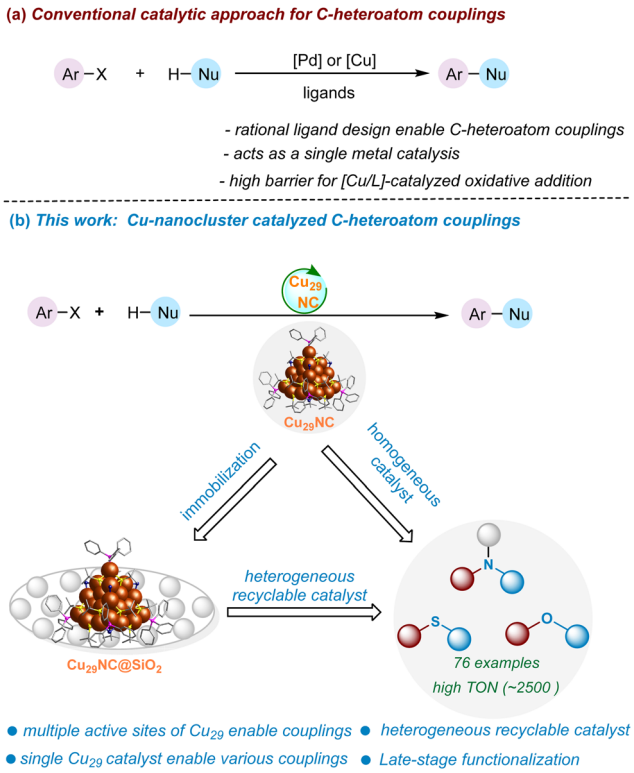

Fig. 1 Catalytic methods for C-heteroatom bond-forming reactions.

Results and discussion

Synthesis and characterizations of Cu_{29} nanocluster

The Cu_{29} cluster was synthesized by a two-step procedure. In brief, the reduction of Cu(I)-S^{t}Bu-PPh$_3$ complex (chloroform solution) by ethanolic solution of sodium borohydride ($NaBH_4$) produced the $Cu_{29}NC$. The synthesis procedure is detailed in the experimental section of the ESI.†

A single crystal of appropriate size was used for single-crystal X-ray diffraction (SCXRD). The cluster crystallizes in a triclinic crystal system with $P\bar{1}$ space group (Table S1, ESI†). The total structure of the Cu_{29} clusters derived from the SCXRD is presented in Fig. 2a. A combined study of SCXRD and mass spectrometry confirms the total molecular formula of the cluster, $[Cu_{29}(S^tBu)_{13}Cl_5(PPh_3)_4H_{10}]^tBuSO_3$ (*vide infra*). The cluster contains a centered-cubooctahedron core (Cu_{13}, Fig. 2b and Fig. S1, ESI†) which is protected by a unique tetrahedral shell, $Cu_{16}S_{13}Cl_5P_4$ (Fig. 2c). The structure contains only one C_1 symmetry axis.

The shell, $Cu_{16}S_{13}Cl_5P_4$, is composed of three different types of motifs, **motif 1** ($Cu_4S_4Cl_2P$), **motif 2** ($Cu_4S_4Cl_2P$), and **motif 3** ($Cu_4S_5Cl_1P$) (Fig. 2d). All the motifs have crown-like structures. **Motif 1** is connected with two units of **motif 2** through two bridging μ_2-Cl whereas **motif 3** is connected to **motif 1** through

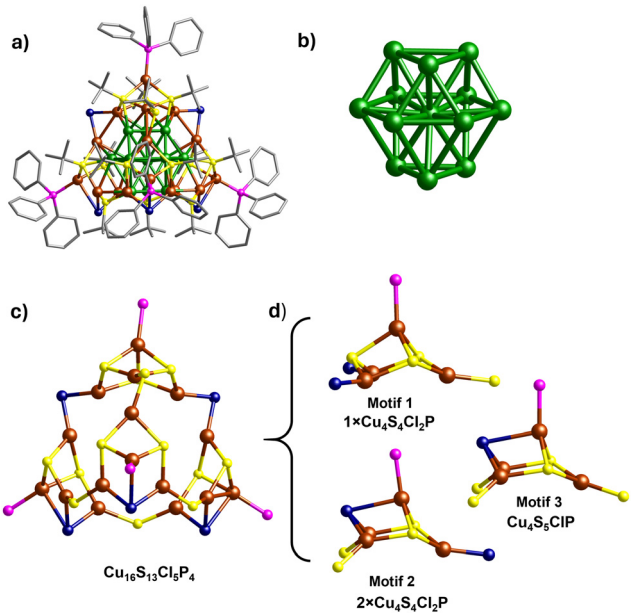

Fig. 2 (a) Molecular structure of $[Cu_{29}(S^tBu)_{13}Cl_5(PPh_3)_4H_{10}]^+$ $Cu_{29}NC$. (b) Cubo octahedron Cu_{13} core. (c) Structure of tetrahedral shell, $Cu_{16}(S^tBu)_{13}Cl_5(PPh_3)_4$. Carbon and hydrogen atoms are omitted for clarity (d) Structures of three distinct types of motifs. Color legend: green, and brown, copper atoms of the Cu_{13} core, and shell, respectively; yellow, sulfur; pink, phosphine; dark blue, chlorine; and gray, carbon.

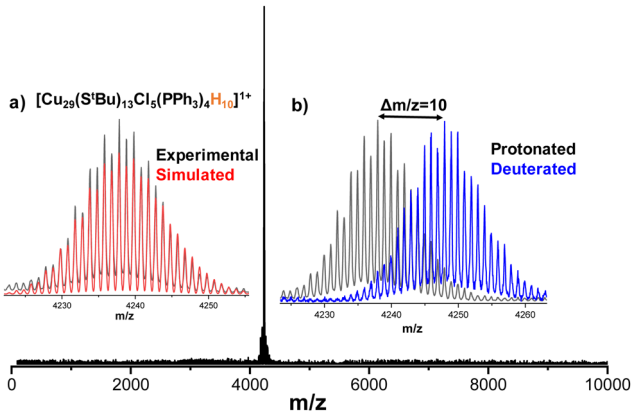

Fig. 3 Positive mode ESI MS spectrum of $[Cu_{29}(S^tBu)_{13}Cl_5(PPh_3)_4H_{10}]^+$ nanocluster. The peak at *m*/*z* 4237.8 corresponds to the molecular ion peak. Insets: (a) Exact matching of experimental (black trace) and simulated (red trace) isotopic distributions confirm the assigned compositions. (b) Comparison of protonated, $[Cu_{29}(S^tBu)_{13}Cl_5(PPh_3)_4H_{10}]^+$, and deuterated, $[Cu_{29}(S^tBu)_{13}Cl_5(PPh_3)_4D_{10}]^+$, molecular ion peaks.

bridging thiolate ligands. On the other hand, two units of **motif 2** and one unit of **motif 3** are interconnected through three bridging thiolate ligands. The interactions of **motifs 1**, **2** and **3** with the Cu_{13} core are quite different. The surface of the Cu_{13} core is composed of six distorted square and eight triangle faces (Fig. S2, ESI†). **Motif 1** occupies one of the triangular faces whereas **motifs 2** and **3** occupy the three-square faces of the Cu_{13} core (Fig. S3, ESI†). Overall, the $Cu_{29}NC$ occupies a tetrahedral shape where the corners of the tetrahedron are occupied by the triphenylphosphine ligands. Three diverse types of thiolate ligand groups are observed in the $Cu_{29}NC$ (Fig. S4, ESI†). Like the thiolate ligands, two types of bridging modes are also observed for the chloride ligands. Two chloride ligands that connect **motif 1** with the two units of **motif 2** have μ_2 bridging mode (μ_2-Cl) and the remaining three chloride ligands have μ_3 bridging mode (μ_3-Cl). It is worth mentioning that such kind of chloride rich (high chloride to thiolate ratio) shell structure is rare in the core–shell nanocluster family. The presence of a higher percentage of chloride ions reduces the crowding of surface copper atoms and, hence, heightens their probability of being involved in catalysis.

Generally, copper nanoclusters contain hydrides.[47,52,55–59] However, it is difficult to locate them using SCXRD for such a larger cluster system. Thus, ESI MS was used to determine the exact composition of the clusters. Details of the sample preparation and instrumental conditions are described in the experimental section of the ESI.† Positive mode ESI MS of the chloroform solution of nanoclusters produced a major peak at *m*/*z* 4237.8 in the mass range of *m*/*z* 20–10000 (Fig. 3). Upon expansion, the peak shows a characteristic separation of $\Delta m/z$ = 1 (Fig. S5, ESI†), which confirms the presence of singly charged (1+) species. The assigned composition for the above-mentioned peak is $[Cu_{29}(S^tBu)_{13}Cl_5(PPh_3)_4H_{10}]^+$. The exact matching of isotopic distributions of experimental (black trace) and simulated (red trace) spectra confirm the assigned composition (Fig. 3a). Furthermore, to verify the number of hydrides, ESI MS of deuterated analogue of $Cu_{29}NC$, Cu_{29D}, was performed. In case of Cu_{29D}, the peak position is shifted by $\Delta m/z$ = 10 due to the replacement of ten hydrogen atoms (*m*/*z* 10) by deuterium atoms (*m*/*z* 20) which further supports the assigned compositions (Fig. 3b). Similar to the reported copper nanoclusters,[52,60] we performed geometry optimizations by DFT calculations to locate the ten hydrides (Fig. S6A, ESI†). Details of the calculations are presented in the experimental section of the ESI.† In order to substantiate the existence of the hydrogen atoms within the NC, a ^2H nuclear magnetic resonance (NMR) analysis was conducted on Cu_{29D} in 950 MHz spectrometer in $CHCl_3$, as illustrated in Fig. S6B (ESI†). These yielded signals originating exclusively from deuterium (D) atoms within the sample and added $CDCl_3$ for calibration. The resultant NMR spectrum exhibited discernible peaks distributed across a range of chemical shift values, ranging from low to high regions. This observation provides compelling evidence for the presence of deuterium atoms within the NC, indicative of their occupancy in diverse chemical environments.

The unique shell structure along with the easily obtainable clean mass spectrum allowed us to study the cluster further using mass spectrometry (Fig. S7 and S8, ESI†). Furthermore, to identify the counter ion, we performed the ESI MS measurement in the negative mode and observed a peak at *m*/*z* 137 (Fig. S9, ESI†). The exact matching of experimental and simulated isotopic distributions confirms the presence of *tert*-butyl sulfonate ($^tBuSO_3^-$) as the counter ion, which is in good agreement with SCXRD data (inset, Fig. S9, ESI†).

The oxidation state of copper atoms holds a fundamental significance in catalysis, which can influence the reactivity and

selectivity. Thus, we performed X-ray photoelectron spectroscopy (XPS) measurements of the solid powder sample to identify the oxidation states of the copper atoms. XPS survey spectrum presented in Fig. S10a (ESI†) confirms the presence of all the expected elements (Cu, S, Cl, C, and P). High-resolution XPS spectra of Cu 2p, S 2p, C 1s, and Cl 2p are presented in Fig. S10b–e (ESI†). Generally, it is difficult to distinguish Cu(0) and Cu(I) as their 2p binding energy are almost similar. Hence, we gathered Cu LMM Auger spectra of Cu(I)–S^{t}Bu thiolate and Cu_{29} cluster (Fig. S11, ESI†). The presence of a sharp peak at 916.3 eV confirms that all the copper atoms in Cu_{29} nanocluster are in +1 oxidation state which is in good agreement with SCXRD and ESI MS analysis.[61] Furthermore, a comparison of Cu LMM Auger spectra Cu(I)-S^{t}Bu thiolate and Cu_{29} cluster is presented in Fig. S11 (ESI†) which also supports the presence of only Cu(I) oxidation state in Cu_{29} nanocluster.

Reaction development

We commenced our investigations with the newly synthesized Cu_{29}NC and tested the cluster in the C–O cross-coupling of *p*-bromobenzonitrile and *p*-cresol. Use of 0.05 mol% of catalyst provided 86% of the desired C–O coupled product (Fig. 4 and Table S2, entry 1, ESI†). Most striking, the reaction can be effectively performed with a catalyst loading of 0.025 mol% still providing the coupled product in 88% yield (Fig. 4, and Table S2, Entry 2, ESI†). The optimal temperature was found to be 90 °C while lower temperature resulted in lower yield (Table S2, entries 3 and 4, ESI†). Further we examined various conditions with respect to catalyst, bases, and solvents to understand and improve the catalytic performance of Cu_{29}NC on the cross-coupling reactions (Table S2, entries 5–12, ESI†). Solvent optimizations indicate that CH_3CN provided more yield in the case of a C–O coupling reaction while DMSO is better for other cross-couplings (C–N and C–S bond formations, see details in Table S3 and S4, ESI†). In order to better understand the catalyst efficacy, optimization studies were performed in the presence of two different electrophiles (*p*-bromobenzonitrile and *p*-bromoanisole) with *p*-cresol as the nucleophile under standard reaction (Fig. 4). As direct comparison, CuCl was investigated as a catalyst instead of Cu_{29}NC (Fig. 4), leading to lower efficiency (~22% yield), which is in line with the previous work.[17,18]

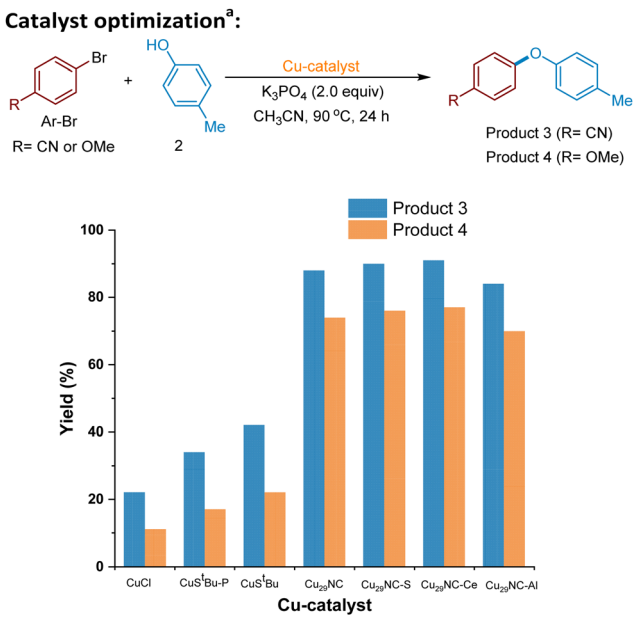

Fig. 4 Catalyst optimization. [a]Conditions: Ar–Br (0.3 mmol), 2 (0.375 mmol), Cu-catalyst used such as 5 mol% of CuCl or CuS^{t}Bu-PPh$_3$, CuS^{t}Bu or 0.025 mol% of Cu_{29}NC or Cu_{29}-Celite S or Cu_{29}NC-CeO_2 or Cu_{29}NC-Al_2O_3), K_3PO_4 (2.0 eq.), and acetonitrile (CH_3CN) (2 mL). The mixture was stirred at 90 °C for 24 h. Yield refers to GC yield using 1,3,5-trimethylbenzene (mesitylene) as the internal standard.

Control experiments demonstrated that the absence of the Cu_{29}NC catalyst or a base resulted in no reaction or trace amounts observed (Table S2, entries 13 and 17, ESI†). Notably, the current Cu_{29}NC catalyst can be supported on different surfaces (Celite S, Celite 545, alumina (γ), CeO_2, and carbon powder) and tested for the C–O coupling reaction. These findings indicate that 0.025 mol% of Cu_{29}-Celite S is an effective C–O cross-coupling catalyst, with similar efficiencies to the unsupported cluster (Fig. 4 and details in ESI†), while also providing higher recyclability than other supports. Furthermore, Cu-complexes, namely Cu(I) S^{t}Bu-PPh$_3$ and Cu(I) S^{t}Bu (precursors for the preparation of Cu_{29}NC), were used as catalysts. However, the desired C–O coupling products (**3** and **4**) were obtained in lower yields with both, activated electrophiles (<42% yield) and unactivated electrophiles (<22% yield) compared to Cu_{29}NC (which yields 88%) (See, Fig. 4). Previously, we used Cu_{61}NC and Cu_{28}NC for photocatalytic C(sp^2)$^-$ Nhet Ullmann–Goldberg coupling[54] and Sonogashira C–C cross-coupling reaction,[52] respectively. In this regard, we performed control experiments with Cu_{61}NC and Cu_{28}NC as catalysts instead of Cu_{29}NC for the current C–O cross-coupling reactions, however, they produced low yields, 58% and 63%, respectively (Table S2, entries 8 and 9, ESI†). Thus, we hypothesize that the differently oriented chloride rich motif structures of Cu_{29}NC plays a key role in this reaction's efficiency.

Recyclable Cu_{29}NC catalyst development

In order to convert the Cu_{29}NC nanocluster into a heterogeneous recyclable catalyst, we aimed to attach the catalyst to a support. Thus, we prepared five different supported clusters (Cu_{29}-Celite S, Cu_{29}-Celite 545, Cu_{29}-alumina (γ), Cu_{29}-CeO_2, and Cu_{29}-carbon powder) and compared the three-reaction parameters, catalyst loading, performance, and leaching, to find the best heterogeneous catalyst. Details of their synthesis are described in the experimental section of the ESI.† The catalyst systems Cu_{29}-Celite S, Cu_{29}-CeO_2, and Cu_{29}-alumina (γ) showed better loading and performance than the remaining two systems (Fig. S12 and S13, ESI†). Interestingly, Cu_{29}–CeO_2 and Cu_{29}-alumina (γ) showed a higher amount of leaching after the 1st cycle, whereas a negligible amount of leaching was observed for Cu_{29}-Celite S (Fig. S14, ESI†). Thus, recyclability was further studied with the Cu_{29}-Celite S system. The diffuse reflectance optical spectrum of the pure Cu_{29} cluster showed

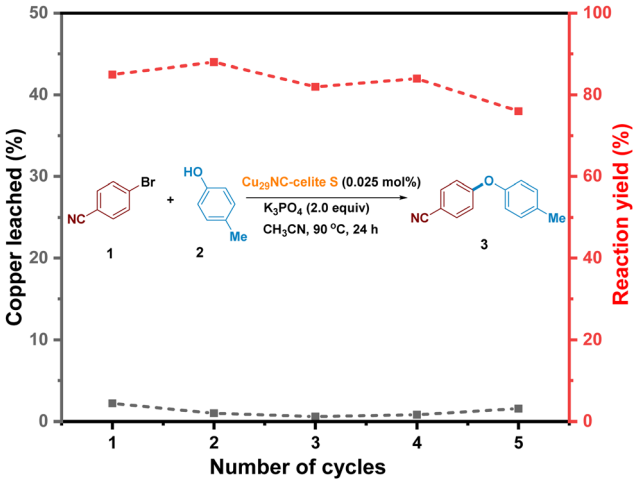

Fig. 5 Recycling of Cu_{29}-Celite S catalyst. Percentage of yield and leaching are denoted with red and black traces, respectively. The amount of leached copper is negligible for each cycle.

two step-like features at 504 and 463 nm (black trace, Fig. S15a, ESI†). These features were also observed for the Cu_{29}-Celite S system (red trace, Fig. S15a, ESI†). A comparison of XPS results confirmed that the oxidation state of Cu atoms remained unaffected during the synthesis of the supported cluster, Cu_{29}-Celite S (Fig. S15b, ESI†). Furthermore, *Z*-contrast scanning transmission electron microscopy (STEM) analysis of Cu_{29}-Celite S showed that the size of the pure Cu_{29} cluster also remained (Fig. S15C, ESI†). All these results showed that the Cu_{29} nanoclusters loaded on Celite S support did not decompose or change shape (Fig. S15, ESI†). It is worth mentioning that the efficiency of this supported catalyst was similar to that of the unsupported form (Fig. 4). Furthermore, we demonstrated that the heterogeneous catalyst could be easily recycled and reused for five cycles with similar activity (Fig. 5, see details in ESI,† Fig. S15). There might be a possibility that the cluster decomposes and releases copper atoms/copper thiolates during the reaction (2nd cycle onwards). However, we detected negligible amounts of the copper in the solution which shows that there is no considerable cluster decomposition during the catalytic reactions (Fig. 5, black trace). In contrast, previous reports on gold clusters have shown that the catalytic efficiency of free clusters is extremely low compared to supported clusters.[62,63] Preheat treatment at around 150 °C[43,64,65] and partial or complete ligand removal are also required to achieve better efficiency in these reports.[43,66] However, our study found that preactivation of the Cu_{29}NC cluster at elevated temperatures is unnecessary, as the performance of both free and supported clusters remains almost the same. Thus, our cluster system provides a synergistic effect between homogeneous and heterogeneous catalysts, setting it apart from other catalytic systems.

Substrates scope

With the optimized conditions and recyclability of the catalyst in hand (Fig. 4, Table S2, ESI†), we set out to explore the scope of the C–O cross-coupling using various aryl/heteroaryl bromides (Fig. 6, heterogeneous Cu_{29}-Celite S (Cu29-S) catalyst is used for those mentioned in bracket). In summary, a wide variety of electron-neutral, electron-donating, and electron-withdrawing aryl bromides react well in the C–O coupling reaction, providing the corresponding C–O arylated products in good to excellent yields (69–93% yields). Typically, electron-rich aryl bromides are poor coupling partners due to a higher energy barrier for the oxidative addition step.[22] Notably, the Cu_{29}NC performs as an efficient catalyst for electron-rich to neutral aryl bromides (4–7, 76–81% yields). In addition, diverse *meta*- and *ortho*-substituted aryl bromides are also amenable to the transformation (9 & 10). Particularly, sterically more hindered 1-bromonaphthalene performed well in this Cu_{29}NC-catalyst process, demonstrating another advancement over previous copper-catalyzed processes.[18] In general, heteroaryl bromides are not good coupling partners in copper catalysis, due to their strong coordination with the metal-catalyst, which may hinder the catalytic activity.[67–69] Remarkably, the current Cu-cluster catalyzed reaction is viable for a series of heteroaryl bromides (12 and 13 and 25 and 26, 77–85% yields). Next, a combination of various phenols and aryl bromides was employed in and the products were obtained in good to excellent yield (15–26). Notably, phenols bearing chloride and bromide at the para position were also well tolerated and gave the corresponding product without affecting the bromine atom (18 and 19, 71–77%), potentially allowing for the subsequent orthogonal functionalization.[70–74] Electron-deficient and heteroaryl phenols are also suitable nucleophiles in this cross-coupling transformation (21 and 26). In addition, phenols containing the unactivated olefin (Eugenol) selectively underwent this reaction and generated their desired C–O coupled product in excellent yield (24 and 25, 84% yields) allowing further functionalization on the olefin bond (*i.e*; Heck-type reactions of eugenol derivatives).[75–78] Moreover, benzylic and aliphatic alcohols were also found to be good coupling nucleophiles in this transformation (27–35). Furthermore, use of ethanol afforded the C–O coupled products in good yields (27, 73% yield). In particular, primary alcohols containing benzylic, CF_3, cyclopentyl, *n*-octanol, and pyridine-substituted alcohols were also good coupling partners with aryl(hetero)-bromides (28–35, 69–89% yields). Interestingly, a terminal olefin substituted linear alcohol is also tolerated in this C–O coupling reaction without affecting the C–C double bond (32, 69% yield), allowing follow-up coupling reactions.[75,76,78]

Mechanistic studies

To define the reaction mechanism, control experiments (Schemes S4 and S5, ESI†) and quantum mechanical calculations were performed. First, a radical trapping experiment was conducted to check for the presence of radical species in the reaction pool. No radical was identified. Further, a radical clock experiment using aryl bromides **36** and *p*-cresol **2** under standard conditions results in the non-cyclized product **37** predominating over the cyclized product **38** (Scheme S4, ESI†). These control experiments indicate that the reaction does not proceed through radical formation. The above results also suggest that

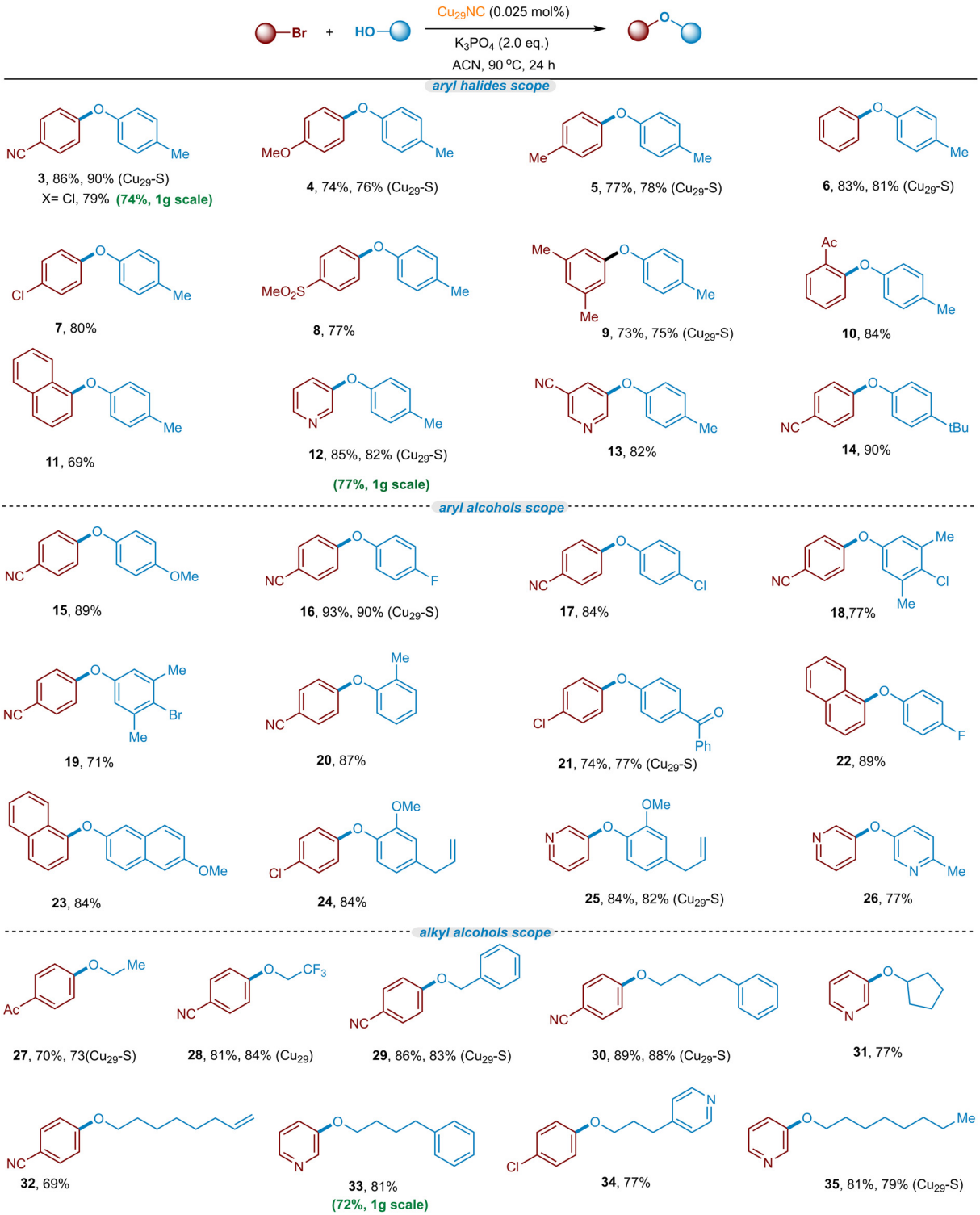

Fig. 6 Substrate scope of aryl halides and alcohols. Standard reaction conditions. Yield of isolated product after purification by column chromatography on a silica gel. (Cu29-S) indicates heterogeneous Cu_{29}-Celite S.

the oxidative addition of Ar–X (X = Br, Cl is operated by a concerted mechanism instead of a single electron transfer (SET). To further discern between concerted oxidative addition and SET pathways we carried out competition experiments. For example, the reaction with a 1 : 1 mixture of 4-chlorobenzonitrile (**1-Cl**) and 1-bromonaphthalene (39) with *p*-cresol as nucleophile, under standard conditions provides a product ratio of 1 : 14.2 (Scheme S5a, ESI†). Despite its lower reduction potential of **1-Cl**, **39** reacts faster, which can be related to the weaker C–Br bond compared to C–Cl. Consistently, a 1 : 1 mixture of **1-Cl** and 4-iodoanisole (40)

leads to a product ratio of 1 : 12.75 (Scheme S5b, ESI†). Overall, these results indicate that conventional two-electron oxidative addition is operative instead of a radical pathway *via* SET.[54,79]

Electronic structure modeling of all possible intermediates along the reaction pathway were performed using a DFT approach[80,81] (refer to ESI† for computational methods). In the DFT study we selected two different electrophiles, 4-bromoanisole and 4-chloroanisole, combined with the nucleophilic partner *p*-cresol. We started by identifying the most active site and elucidating an ensemble effect, which is the involvement of more than one Cu atom in Cu_{29}NC. To achieve this goal, we have relied on the thermodynamic feasibility of the first step, which is $(Cu)_{29}$–OAr formation *via* deprotonation by K_3PO_4. Different $(Cu)_{29}$–OAr intermediates were modeled (Fig. 7), by considering all the structurally different surface Cu-atoms on **motifs 1–3** (Fig. 2). In addition to nine intermediates showing the nucleophile –OAr interacting with one single Cu atom (structures $\mathbf{A_1}$–$\mathbf{A_6}$ and $\mathbf{A_8}$–$\mathbf{A_{10}}$ in Fig. 7), we also identified one intermediate with the –OAr fragment bridging two adjacent Cu atoms, one of which is terminal (structure $\mathbf{A_7}$ in Fig. 7). Intermediate $\mathbf{A_7}$ is identified as the most stable one, suggesting for an ensemble effect favoring the initial activation of Cu_{29}NC. Other attempts to locate low energy structures with the –OAr fragment bridging two adjacent Cu atoms failed. Overall, the higher stability of structures $\mathbf{A_4}$–$\mathbf{A_7}$ indicate that **motif 2** has more active Cu atoms compared to **motifs 1 and 3**.

All the intermediates along the reaction pathway and their relative energies are displayed in Fig. 8 involving 4-bromoanisole, and in Fig. S17 (refer to ESI†) for chloro analogue. As discussed above, the reaction starts with formation of the Cu–Nu bond in the presence of a strong base, K_3PO_4, which is exergonic by 138.1 kcal mol^{-1}. The resulting intermediate $\mathbf{A_7}$ undergoes oxidative addition of 4-bromoanisole, since the alternative SET step is endergonic by 104.7 kcal mol^{-1} and can thus be excluded (Fig. S18, ESI†), consistently with the experimental evidence.

Within the conventional 2e oxidative addition scheme, two possible pathways (green *vs.* red paths in Fig. 8 were considered depending on the mechanism of Ar–Br activation. The first we considered involves a bimetallic mode of activation, with the Ar and Br moieties bound to two vicinal Cu atoms (green line in Fig. 8), is endergonic by 20.3 kcal mol^{-1} and leads to intermediate $\mathbf{B_{Br}}$. The next step, debromination from $\mathbf{B_{Br}}$ results in the cationic intermediate $\mathbf{C_{Br}}$ with an energy gain of 32.8 kcal mol^{-1}. Finally, highly exergonic reductive elimination from $\mathbf{C_{Br}}$ results in the desired product and regenerates the starting Cu_{29}NC which is ready to start another catalytic cycle.

The second pathway we considered involves a standard monometallic oxidative addition of Ar–Br at a single Cu-atom (red line in Fig. 8), leading to the intermediate $\mathbf{B_{Br}}'$, which is 18.3 kcal mol^{-1} more unstable than the bimetallic intermediate $\mathbf{B_{Br}}$. Consistently, the following debrominated intermediate, $\mathbf{C_{Br}}'$, is higher in energy than $\mathbf{C_{Br}}$ by 12.3 kcal mol^{-1}. Overall, the above results indicate that the pathway with bimetallic oxidative addition (green line) is more viable than the corresponding monometallic one (red line). Considering the initial reaction of Cu_{29}NC with the HO–Ar nucleophile, also favored by the presence of two nearby Cu atoms, our calculations indicate the role of an ensemble effect in favoring the whole reaction

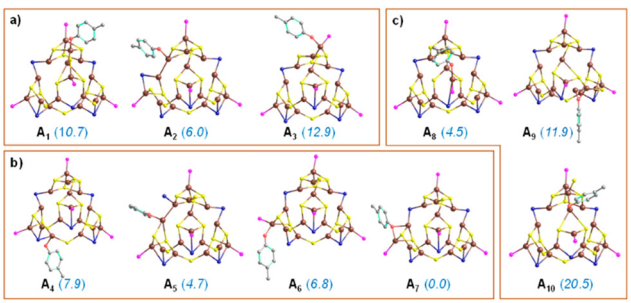

Fig. 7 DFT optimized structures and relative energies (in kcal mol^{-1}) of $(Cu)_{29}$–OAr complexes varying the active Cu-atom in three different regions: (a) **motif 1**, (b) **motif 2**, and (c) **motif 3**. Only surface Cu atoms are projected, and H atoms are omitted for clarity. The energy values are at the PBE-D3 level of theory using implicit solvation model in acetonitrile.

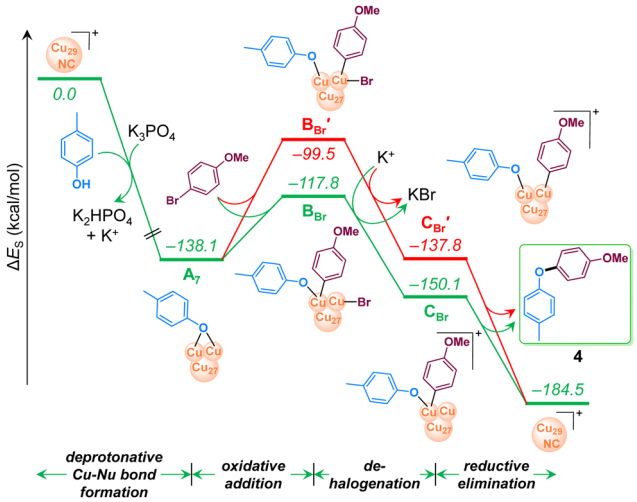

Fig. 8 Computed energy profile of Cu_{29}-NC catalyzed C–O coupling reaction of *p*-cresol using 4-bromoanisole. For energy convention, refer to Fig. 7.

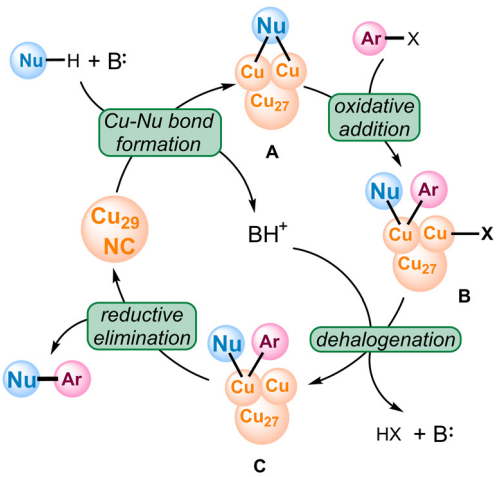

Scheme 1 Proposed catalytic cycle.

pathway. Consistently, the computed energy profile for 4-chloroanisole (Fig. S17 in ESI†) resembles that of 4-bromoanisole (Fig. 8). To further acquire more insight into the kinetics involved, a linear one-dimensional scan analysis of the potential energy surface (PES) was conducted on the reaction rate-limiting step, oxidative addition of ArBr to $\mathbf{A_7}$ (Fig. S19 in ESI†). By creating a series of "images" along the bond (C–Br) breaking during the reaction with a specific increment of the distance between the C and Br with all atoms relaxed, an energy profile was described from which the energy barrier was predicted to be lower towards the formation of $\mathbf{B_{Br}}$ compared to that of $\mathbf{B_{Br}}'$. The nudged elastic band and dimer methods were tested and deemed unfeasible due to the large size of the system.

Finally, based on our control experiments and computational results, we propose the catalytic cycle of the $Cu_{29}NC$ catalyzed C-heteroatom coupling reaction, shown in Scheme 1.

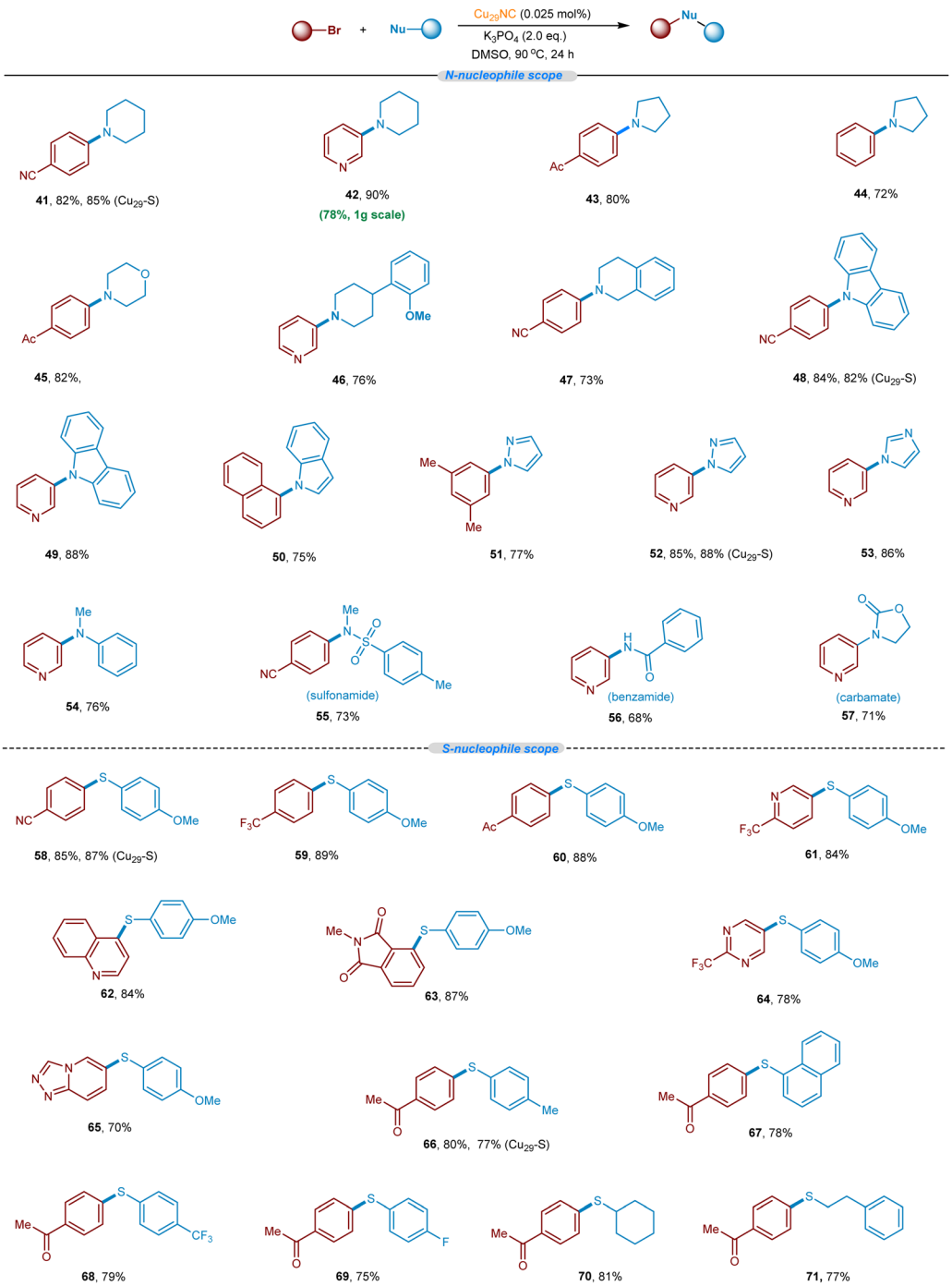

Fig. 9 Substrate scope of *N*-nucleophiles and *S*-nucleophiles with aryl halides. Standard reaction conditions. Yield of isolated product after purification by column chromatography on a silica gel. (Cu29-S) indicates heterogeneous Cu_{29}-Celite S.

The mechanism includes four fundamental steps: deprotonative Cu–Nu bond formation, oxidative addition, dehalogenation, and reductive elimination to liberate the product. Notably, though the reaction occurs at the terminal Cu of **motif 2**, the neighboring Cu also plays a significant role during the reaction pathway. As a result, the ensemble effect is visible in the DFT calculations, which clearly distinguishes the catalytic behavior of a nanocluster from single metal catalysis.

Extended substrates scope

After successfully demonstrating the C–O cross-coupling reaction, we aimed to explore the C–N and C–S cross-coupling reaction of N & S-nucleophiles with aryl bromides (Fig. 9 and optimization condition see Tables S3 and S4, ESI†). To summarize, secondary aliphatic amines such as pyrrolidine, piperidine, and morpholine readily undergo the desired C–N cross-coupling with various aryl bromides including pyridinyl aryl bromides (41–47, 72–90% yields). This Cu-cluster catalysis is also applicable to C–N cross-couplings of N-heterocycles with various aryl bromide electrophiles. For example, carbazole, indole, pyrazole, and imidazole are found to be competent nucleophiles in this cross-coupling reaction, providing desired C–N arylated products in excellent yield (48–53). Other *N*-nucleophiles such as *N*-alkylaniline, sulfonyl amines, benzamide, and oxazolidin-2-one,

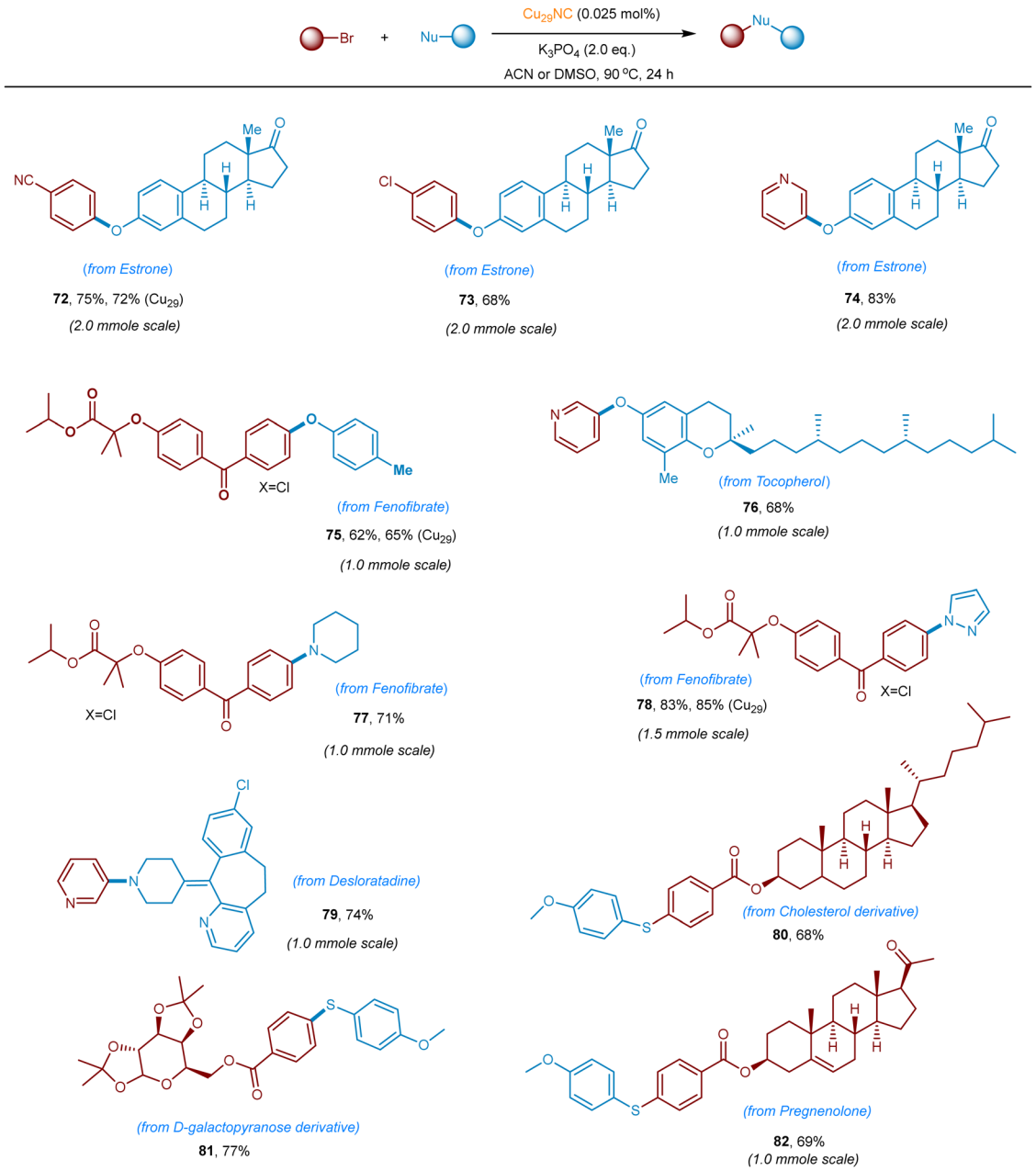

Fig. 10 Late-stage functionalization of complex organic and drug molecules. Standard reaction conditions. Yield of isolated product after purification by column chromatography on a silica gel. (Cu29-S) indicates heterogeneous Cu_{29}-Celite S.

also reacted well (54–57, 68–76% yields). Besides, we set out to explore the *S*-nucleophiles with aryl bromides under the optimized Cu_{29}NC catalytic conditions. It is worth noting that, electron-rich and electron-poor thiophenol derivatives readily underwent C–S coupling and the products were isolated in good to excellent yields (58–71, 70–89% yields). Heteroaryl bromides were found to be well-suitable coupling electrophiles in combination with thiophenol nucleophiles (61–65). An aliphatic thioalcohol was also successfully applied (70 and 71).

To further highlight the synthetic utility and generality of this new Cu_{29}NC catalytic system, late-stage functionalization of structurally complex organic molecules or drug-like molecules *via* C–O, C–N, and C–S bond-forming reactions was demonstrated. As summarized in Fig. 10 natural products containing *O*-nucleophiles such as estrone, tocopherol, are selectively coupled with aryl(hetero)-bromides without affecting other functionalities. The C–O, C–N, & C–S couplings was also accomplished on 1.0 to 2.0 mmole scale (72–82, 65–85% yields). Fenofibrate was reacted with *p*-cresol, piperidine, and pyrazole, and the corresponding coupled products isolated in very good yield (75 and 77–78, 65–85% yields). Importantly, N-heterocylce containing desloratadine is smoothly coupled with 3-bromopyridine to afford the C–N coupled product (79, 74% yield). Furthermore, *S*-nucleophile-containing drugs/complex structures can be late-stage functionalized with aryl bromides, delivering the corresponding products in good to excellent yields (80–82). Collectively, the current Cu_{29}NC catalysis is viable for the efficient C-heteroatom bond-forming reactions of pharmaceutical molecules bearing multiple functional groups and is thus attractive for pharmaceuticals synthesis and late-stage drug modification or functionalization.

Conclusions

In summary, a core–shell nanocluster, $[Cu_{29}(S^tBu)_{13}Cl_5(PPh_3)_4H_{10}]^tBuSO_3$ with a unique shell structure has been synthesized. The shell, $[Cu_{16}(S^tBu)_{13}Cl_5(PPh_3)_4]$, is composed of three different types of motifs; **motif 1** ($Cu_4S_4Cl_2P$), **motif 2** ($Cu_4S_4Cl_2P$), and **motif 3** ($Cu_4S_5Cl_1P$). The cluster has been utilized as a versatile catalyst in various C-heteroatom coupling reactions of structurally diverse aryl(hetero) halides with a broad range of nucleophiles (alcohols, amines, sulphur, and amides), including, late-stage functionalization of complex organic molecules or pharmaceuticals bearing multiple functional groups. The DFT-based mechanistic study along with control experiments provided insight into the reaction mechanism. Our calculations suggest that the active sites of **motif 2** show better catalytic activity than **motifs 1 and 3**. Further studies showed that the participation of multiple neighboring active sites at the different stages of the reactions play a crucial role for catalytic performance of the Cu_{29}NC. The involvement of multiple active sites of Cu_{29}NC substantially lowered the energy barrier of oxidative addition of aryl halide which was found to be the rate-limiting step. Furthermore, the supported Cu_{29}NC system was shown to exhibit recyclability without significant loss in the catalytic activity. We anticipate that the new insights gained from this study will be instrumental in the design, synthesis, and applications of more effective nanocluster catalysts.

Conflicts of interest

There are no conflicts to declare.

Acknowledgements

This work was supported by King Abdullah University of Science and Technology (KAUST).

Notes and references

1 N. Schneider, D. M. Lowe, R. A. Sayle, M. A. Tarselli and G. A. Landrum, *J. Med. Chem.*, 2016, **59**, 4385–4402.
2 I. Ghosh, N. Shlapakov, T. A. Karl, J. Düker, M. Nikitin, J. V. Burykina, V. P. Ananikov and B. König, *Nature*, 2023, **619**, 87–93.
3 S. D. Roughley and A. M. Jordan, *J. Med. Chem.*, 2011, **54**, 3451–3479.
4 E. Vitaku, D. T. Smith and J. T. Njardarson, *J. Med. Chem.*, 2014, **57**, 10257–10274.
5 G. Evano, J. Wang and A. Nitelet, *Org. Chem. Front.*, 2017, **4**, 2480–2499.
6 T. Qin, B. Liu, K. Zhu, Z. Luo, Y. Huang, C. Pan and L. Wang, *TrAC, Trends Anal. Chem.*, 2018, **102**, 259–271.
7 W. Schutyser, T. Renders, S. Van den Bosch, S. F. Koelewijn, G. T. Beckham and B. F. Sels, *Chem. Soc. Rev.*, 2018, **47**, 852–908.
8 P. Ruiz-Castillo and S. L. Buchwald, *Chem. Rev.*, 2016, **116**, 12564–12649.
9 C. H. Burgos, T. E. Barder, X. Huang and S. L. Buchwald, *Angew. Chem., Int. Ed.*, 2006, **45**, 4321–4326.
10 G. Mann, C. Incarvito, A. L. Rheingold and J. F. Hartwig, *J. Am. Chem. Soc.*, 1999, **121**, 3224–3225.
11 S. D. McCann, E. C. Reichert, P. L. Arrechea and S. L. Buchwald, *J. Am. Chem. Soc.*, 2020, **142**, 15027–15037.
12 J. D. Laffoon, V. S. Chan, M. G. Fickes, B. Kotecki, A. R. Ickes, J. Henle, J. G. Napolitano, T. S. Franczyk, T. B. Dunn, D. M. Barnes, A. R. Haight, R. F. Henry and S. Shekhar, *ACS Catal.*, 2019, **9**, 11691–11708.
13 F. Ullmann and P. Sponagel, *Ber. Dtsch. Chem. Ges.*, 1905, **38**, 2211–2212.
14 G. Evano, N. Blanchard and M. Toumi, *Chem. Rev.*, 2008, **108**, 3054–3131.
15 F. Monnier and M. Taillefer, *Angew. Chem., Int. Ed.*, 2009, **48**, 6954–6971.
16 D. S. Surry and S. L. Buchwald, *Chem. Sci.*, 2010, **1**, 13–31.
17 S.-T. Kim, M. J. Strauss, A. Cabré and S. L. Buchwald, *J. Am. Chem. Soc.*, 2023, **145**, 6966–6975.
18 R. Ray and J. F. Hartwig, *Angew. Chem., Int. Ed.*, 2021, **60**, 8203–8211.
19 S. Bhunia, G. G. Pawar, S. V. Kumar, Y. Jiang and D. Ma, *Angew. Chem., Int. Ed.*, 2017, **56**, 16136–16179.

20 Z. Chen, Y. Jiang, L. Zhang, Y. Guo and D. Ma, *J. Am. Chem. Soc.*, 2019, **141**, 3541–3549.
21 S. Bhunia, S. De and D. Ma, *Org. Lett.*, 2022, **24**, 1253–1257.
22 Q. Yang, Y. Zhao and D. Ma, *Org. Process Res. Dev.*, 2022, **26**, 1690–1750.
23 C. Sambiagio, S. P. Marsden, A. J. Blacker and P. C. McGowan, *Chem. Soc. Rev.*, 2014, **43**, 3525–3550.
24 S. Daly, M. F. Haddow, A. G. Orpen, G. T. A. Rolls, D. F. Wass and R. L. Wingad, *Organometallics*, 2008, **27**, 3196–3202.
25 H.-J. Cristau, P. P. Cellier, S. Hamada, J.-F. Spindler and M. Taillefer, *Org. Lett.*, 2004, **6**, 913–916.
26 N. Xia and M. Taillefer, *Chem. – Eur. J.*, 2008, **14**, 6037–6039.
27 A. Shafir, P. A. Lichtor and S. L. Buchwald, *J. Am. Chem. Soc.*, 2007, **129**, 3490–3491.
28 K. L. Jones, A. Porzelle, A. Hall, M. D. Woodrow and N. C. O. Tomkinson, *Org. Lett.*, 2008, **10**, 797–800.
29 G. V. Smith and F. Notheisz, in *Heterogeneous Catalysis in Organic Chemistry*, ed. G. V. Smith and F. Notheisz, Academic Press, San Diego, 1999, pp. 1–28, DOI: **10.1016/B978-012651645-6/50001-9**.
30 B. M. Trost, *Transition Met. Org. Synth.*, 2004, 2–14, DOI: **10.1002/9783527619405.ch1a**.
31 S. Wu, R. Snajdrova, J. C. Moore, K. Baldenius and U. T. Bornscheuer, *Angew. Chem., Int. Ed.*, 2021, **60**, 88–119.
32 L. Rout, S. Jammi and T. Punniyamurthy, *Org. Lett.*, 2007, **9**, 3397–3399.
33 Y. S. Panova, A. S. Kashin, M. G. Vorobev, E. S. Degtyareva and V. P. Ananikov, *ACS Catal.*, 2016, **6**, 3637–3643.
34 S. Jammi, S. Sakthivel, L. Rout, T. Mukherjee, S. Mandal, R. Mitra, P. Saha and T. Punniyamurthy, *J. Org. Chem.*, 2009, **74**, 1971–1976.
35 M. B. Gawande, A. Goswami, F.-X. Felpin, T. Asefa, X. Huang, R. Silva, X. Zou, R. Zboril and R. S. Varma, *Chem. Rev.*, 2016, **116**, 3722–3811.
36 J. Oliver-Messeguer, L. Liu, S. García-García, C. Canós-Giménez, I. Domínguez, R. Gavara, A. Doménech-Carbó, P. Concepción, A. Leyva-Pérez and A. Corma, *J. Am. Chem. Soc.*, 2015, **137**, 3894–3900.
37 B. Mondal, K. Basu, R. Jana, P. Mondal, B. Hansda, A. Datta and A. Banerjee, *ACS Appl. Nano Mater.*, 2022, **5**, 7932–7943.
38 L. L. Chng, N. Erathodiyil and J. Y. Ying, *Acc. Chem. Res.*, 2013, **46**, 1825–1837.
39 Y. Du, H. Sheng, D. Astruc and M. Zhu, *Chem. Rev.*, 2020, **120**, 526–622.
40 I. Chakraborty and T. Pradeep, *Chem. Rev.*, 2017, **117**, 8208–8271.
41 R. Jin, C. Zeng, M. Zhou and Y. Chen, *Chem. Rev.*, 2016, **116**, 10346–10413.
42 G. Li, H. Abroshan, C. Liu, S. Zhuo, Z. Li, Y. Xie, H. J. Kim, N. L. Rosi and R. Jin, *ACS Nano*, 2016, **10**, 7998–8005.
43 R. Jin, G. Li, S. Sharma, Y. Li and X. Du, *Chem. Rev.*, 2021, **121**, 567–648.
44 S. Wang, L. Tang, B. Cai, Z. Yin, Y. Li, L. Xiong, X. Kang, J. Xuan, Y. Pei and M. Zhu, *J. Am. Chem. Soc.*, 2022, **144**, 3787–3792.
45 W. Zhu, S. Zhang, W. Fan, Y. Yang, H. Zhao, W. Fei, H. Bi, J. He, M.-B. Li and Z. Wu, *Precis. Chem.*, 2023, **1**, 175–182.
46 A. Ghosh, O. F. Mohammed and O. M. Bakr, *Acc. Chem. Res.*, 2018, **51**, 3094–3103.
47 S. Lee, M. S. Bootharaju, G. Deng, S. Malola, W. Baek, H. Häkkinen, N. Zheng and T. Hyeon, *J. Am. Chem. Soc.*, 2020, **142**, 13974–13981.
48 C. Sun, N. Mammen, S. Kaappa, P. Yuan, G. Deng, C. Zhao, J. Yan, S. Malola, K. Honkala, H. Häkkinen, B. K. Teo and N. Zheng, *ACS Nano*, 2019, **13**, 5975–5986.
49 A. W. Cook, Z. R. Jones, G. Wu, S. L. Scott and T. W. Hayton, *J. Am. Chem. Soc.*, 2018, **140**, 394–400.
50 C. Zhang, Z. Wang, W.-D. Si, L. Wang, J.-M. Dou, Z.-Y. Gao, C.-H. Tung and D. Sun, *ACS Nano*, 2022, **16**, 9598–9607.
51 A. Sagadevan, A. Ghosh, P. Maity, O. F. Mohammed, O. M. Bakr and M. Rueping, *J. Am. Chem. Soc.*, 2022, **144**, 12052–12061.
52 S. Nematulloev, A. Sagadevan, B. Alamer, A. Shkurenko, R. Huang, J. Yin, C. Dong, P. Yuan, K. E. Yorov, A. A. Karluk, W. J. Mir, B. E. Hasanov, M. Nejib Hedhili, N. M. Halappa, M. Eddaoudi, O. F. Mohammed, M. Rueping and O. M. Bakr, *Angew. Chem., Int. Ed.*, 2023, **62**, e202303572.
53 C. Dong, R.-W. Huang, A. Sagadevan, P. Yuan, L. Gutiérrez-Arzaluz, A. Ghosh, S. Nematulloev, B. Alamer, O. F. Mohammed, I. Hussain, M. Rueping and O. M. Bakr, *Angew. Chem., Int. Ed.*, 2023, **62**, e202307140.
54 A. Sagadevan, A. Ghosh, P. Maity, O. F. Mohammed, O. M. Bakr and M. Rueping, *J. Am. Chem. Soc.*, 2022, **144**, 12052–12061.
55 A. Ghosh, R.-W. Huang, B. Alamer, E. Abou-Hamad, M. N. Hedhili, O. F. Mohammed and O. M. Bakr, *ACS Mater. Lett.*, 2019, **1**, 297–302.
56 C. Dong, R.-W. Huang, C. Chen, J. Chen, S. Nematulloev, X. Guo, A. Ghosh, B. Alamer, M. N. Hedhili, T. T. Isimjan, Y. Han, O. F. Mohammed and O. M. Bakr, *J. Am. Chem. Soc.*, 2021, **143**, 11026–11035.
57 Y. Bao, X. Wu, B. Yin, X. Kang, Z. Lin, H. Deng, H. Yu, S. Jin, S. Chen and M. Zhu, *Chem. Sci.*, 2022, **13**, 14357–14365.
58 S. Biswas, S. Hossian, T. Kosaka, J. Sakai, D. Arima, Y. Niihori, M. Mitsui, D.-E. Jiang, S. Das, S. Wang and Y. Negishi, *Chem. Commun.*, 2023, **59**, 9336–9339.
59 J. O. Tellechea, C. Lima, D. Choi, D. Salazar, M. Samiei, A. Keoseyan, E. Vinogradova, F. Yan, D. Wherritt, M. M. Alvarez and G. Baghdasarian, *AAAFM Energy Mater.*, 2020, **1**, 16–26.
60 S. Wang, Z. Wu, S. Dai and D.-E. Jiang, *Angew. Chem., Int. Ed.*, 2021, **60**, 12289–12292.
61 R.-W. Huang, J. Yin, C. Dong, A. Ghosh, M. J. Alhilaly, X. Dong, M. N. Hedhili, E. Abou-Hamad, B. Alamer, S. Nematulloev, Y. Han, O. F. Mohammed and O. M. Bakr, *J. Am. Chem. Soc.*, 2020, **142**, 8696–8705.
62 H. Shen, Q. Wu, S. Malola, Y.-Z. Han, Z. Xu, R. Qin, X. Tang, Y.-B. Chen, B. K. Teo, H. Häkkinen and N. Zheng, *J. Am. Chem. Soc.*, 2022, **144**, 10844–10853.
63 G. Li, C. Zeng and R. Jin, *J. Am. Chem. Soc.*, 2014, **136**, 3673–3679.
64 G. Li and R. Jin, *J. Am. Chem. Soc.*, 2014, **136**, 11347–11354.
65 G. Li, D.-e Jiang, C. Liu, C. Yu and R. Jin, *J. Catal.*, 2013, **306**, 177–183.

66 K. Sakamoto, S. Masuda, S. Takano and T. Tsukuda, *ACS Catal.*, 2023, **13**, 3263–3271.
67 X. A. F. Cook, A. de Gombert, J. McKnight, L. R. E. Pantaine and M. C. Willis, *Angew. Chem., Int. Ed.*, 2021, **60**, 11068–11091.
68 M. N. Lavagnino, T. Liang and D. W. C. MacMillan, *Proc. Natl. Acad. Sci. U. S. A.*, 2020, **117**, 21058–21064.
69 A. C. Sather and T. A. Martinot, *Org. Process Res. Dev.*, 2019, **23**, 1725–1739.
70 R. Chinchilla and C. Nájera, *Chem. Soc. Rev.*, 2011, **40**, 5084–5121.
71 A. Hossain, A. Bhattacharyya and O. Reiser, *Science*, 2019, **364**, eaav9713.
72 A. Sagadevan and K. C. Hwang, *Adv. Synth. Catal.*, 2012, **354**, 3421–3427.
73 D. Roy and Y. Uozumi, *Adv. Synth. Catal.*, 2018, **360**, 602–625.
74 A. Sagadevan, A. Charitou, F. Wang, M. Ivanova, M. Vuagnat and M. F. Greaney, *Chem. Sci.*, 2020, **11**, 4439–4443.
75 A. Deb, S. Bag, R. Kancherla and D. Maiti, *J. Am. Chem. Soc.*, 2014, **136**, 13602–13605.
76 S.-S. Wang and G.-Y. Yang, *Catal. Sci. Technol.*, 2016, **6**, 2862–2876.
77 S. Reddy Chidipudi, M. D. Wieczysty, I. Khan and H. W. Lam, *Org. Lett.*, 2013, **15**, 570–573.
78 P.-Z. Wang, Y. Gao, J. Chen, X.-D. Huan, W.-J. Xiao and J.-R. Chen, *Nat. Commun.*, 2021, **12**, 1815.
79 J. W. Tye, Z. Weng, A. M. Johns, C. D. Incarvito and J. F. Hartwig, *J. Am. Chem. Soc.*, 2008, **130**, 9971–9983.
80 G. Kresse and J. Furthmüller, *Comput. Mater. Sci.*, 1996, **6**, 15–50.
81 G. Kresse and J. Hafner, *Phys. Rev. B: Condens. Matter Mater. Phys.*, 1994, **49**, 14251–14269.